Directional perfect absorption using deep subwavelength low-permittivity films

Ting S. Luk,[1,2,*,‡] Salvatore Campione,[1,2,†,‡] Iltai Kim,[1,2,§] Simin Feng,[3] Young Chul Jun,[4] Sheng Liu,[1,2] Jeremy B. Wright,[1] Igal Brener,[1,2] Peter B. Catrysse,[5] Shanhui Fan,[5] and Michael B. Sinclair[1]

[1]*Sandia National Laboratories, P.O. Box 5800, Albuquerque, New Mexico 87185, USA*

[2]*Center for Integrated Nanotechnologies, Sandia National Laboratories, P.O. Box 5800, Albuquerque, New Mexico 87185, USA*

[3]*Naval Surface Warfare Center Dahlgren Division, 18444 Frontage Road, Dahlgren, Virginia 22448, USA*

[4]*Department of Physics, Inha University, Incheon 402-751, Republic of Korea*

[5]*Edward L. Ginzton Laboratory, Stanford University, Stanford, California 94305-4088, USA*

(Received 14 May 2014; published 11 August 2014)

We experimentally demonstrate single beam directional perfect absorption (to within experimental accuracy) of *p*-polarized light in the near-infrared using unpatterned, deep subwavelength films of indium tin oxide (ITO) on Ag. The experimental perfect absorption occurs slightly above the epsilon-near-zero (ENZ) frequency of ITO, where the permittivity is less than 1 in magnitude. Remarkably, we obtain perfect absorption for films whose thickness is as low as $\sim 1/50$th of the operating free-space wavelength and whose single pass attenuation is only $\sim 5\%$. We further derive simple analytical conditions for perfect absorption in the subwavelength-film regime that reveal the constraints that the thin layer permittivity must satisfy if perfect absorption is to be achieved. Then, to get a physical insight on the perfect absorption properties, we analyze the eigenmodes of the layered structure by computing both the real-frequency/complex-wavenumber and the complex-frequency/real-wavenumber modal dispersion diagrams. These analyses allow us to attribute the experimental perfect absorption condition to the crossover between bound and leaky behavior of one eigenmode of the layered structure. Both modal methods show that perfect absorption occurs at a frequency slightly larger than the ENZ frequency, in agreement with experimental results, and both methods predict a second perfect absorption condition at higher frequencies, attributed to another crossover between bound and leaky behavior of the same eigenmode. Our results greatly expand the list of materials that can be considered for use as ultrathin perfect absorbers and provide a methodology for the design of absorbing systems at any desired frequency.

DOI: 10.1103/PhysRevB.90.085411 PACS number(s): 42.25.Bs, 52.25.Os, 78.20.−e

I. INTRODUCTION

For many applications, such as energy conversion, optical modulation, spectral filtering, and sensing, it is desirable to maximize the efficiency of photon absorption for specific conditions of wavelength and incidence angle. Furthermore, the ability to absorb a large fraction of an incoming optical field in an extremely thin film is beneficial for processes such as photovoltaic energy conversion where carrier extraction efficiency is better for thinner films or for devices such as bolometers that require large absorption with small thermal mass. One approach that has been successful in this regard is the use of structured materials such as diffraction gratings and metamaterials [1–10]. In these systems, absorption enhancements arise from the enhanced electromagnetic near-fields that occur at the resonant frequencies of the structures. Another approach that has been investigated is based on critical coupling to the surface plasmon modes of planar metal–dielectric–metal structures [11,12]. A less explored strategy relies on tailoring stratified dielectric media, in which at least one layer exhibits some loss, to exhibit perfect absorption (PA), a process in which (analytically) 100% of light is absorbed in a medium. Such a possibility for wavelength-scale-thick films was recognized quite some time ago, with a number of theoretical papers [13–15] and one experimental paper [16] devoted to the elucidation of this process (though it was not termed PA in these papers). Recently, the PA concept was explored in the context of laser cavities, leading to the so-called coherent PA [17,18]. Still more recently, the intriguing possibility that PA can be achieved using deep subwavelength films of highly lossy, high-permittivity materials on a variety of substrates has been proposed and experimentally verified [19–21]. It is thus of interest to inquire under what conditions similar results can be achieved with deep subwavelength films of low-permittivity materials. Although not discussing PA, the theoretical results of Godwin and Mueller [22] pointed to the possibility that PA could be achieved near the plasma frequency of a layer of diluted plasma backed by a metal. Similarly, Harbecke *et al.* [23] theoretically showed strong absorption above the SiO_2 longitudinal optical phonon frequency in metal-backed films. In addition, a theoretical analysis of PA in the context of an anisotropic epsilon-near-zero (ENZ) metamaterial has recently appeared [24].

In this paper, we present in Sec. II an experimental demonstration of PA for deep subwavelength films of indium tin oxide (ITO) on metal substrates (Ag) at frequencies just above the ENZ frequency, where both the real and the imaginary parts of the ITO permittivity are less than 1. We find that the incidence angle for PA increases as the ITO thickness decreases and that

*Corresponding author: tsluk@sandia.gov

†Corresponding author: sncampi@sandia.gov

‡These authors contributed equally to this paper and are joint first authors.

§Current address: School of Engineering & Computing Science, Texas A&M University-Corpus Christi, Corpus Christi, Texas 78412, USA.

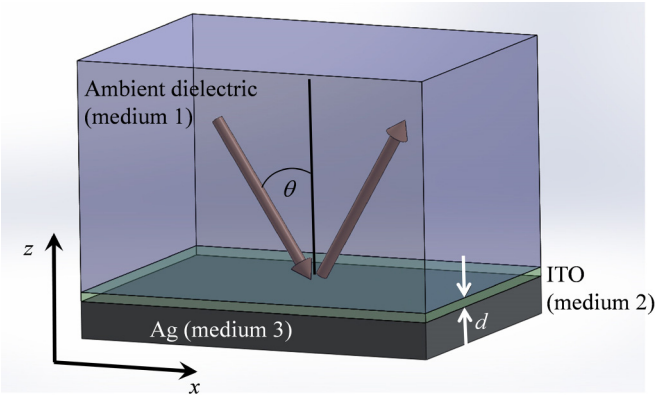

FIG. 1. (Color online) Schematic depiction of a three-medium structure comprising an ambient dielectric (medium 1), a subwavelength ITO layer of thickness d (medium 2), and a metallic substrate (medium 3).

PA can be obtained even when the ITO thickness is decreased to 24 nm ($\sim$1/50th of the free space wavelength of 1.15 μm). We present a simple theoretical analysis of the PA process in Sec. III, obtained within the perfect electrical conductor approximation for the metal substrate, which leads to a set of design equations highlighting the constraints that the thin layer permittivity must satisfy if PA is to be obtained in the subwavelength limit. These equations show that as the real part of the permittivity of the thin layer approaches zero, the film thickness required for PA decreases with decreasing loss in the film—in stark contrast with conventional absorbers, which require larger thicknesses as the material loss is decreased, but in agreement with previous investigations dealing with the well-known ENZ PA [23]. We then analyze in Secs. IV and V the behavior of the electromagnetic eigenmodes of the layered structure and compute the modal dispersion diagrams for both the real-frequency/complex-wavenumber and the complex-frequency/real-wavenumber pictures. These two viewpoints are shown to be self-consistent, and both indicate that the PA condition occurs close to the ENZ frequency at the crossover between bound and leaky behavior of one eigenmode of the system. At these special points, the field structure of the mode becomes indistinguishable from that of a totally absorbed incident plane wave [25]. The modal analysis also reveals the existence of a second PA condition for the ITO thin films at higher frequencies attributed to another crossover of the same eigenmode, which has been numerically verified using the three-medium Fresnel equation [26].

II. EXPERIMENTAL DEMONSTRATION OF PA IN ULTRATHIN, LOW-PERMITTIVITY FILMS

Our experimental demonstration of PA in ultrathin, low-permittivity films utilizes the three-medium structure shown in Fig. 1. It comprises a glass substrate (ambient dielectric, medium 1), an ultrathin ITO layer (medium 2), and an optically thick Ag capping layer (medium 3). For the reflectivity measurements, the optical waves are incident on the ITO film from the glass substrate side. The ITO films were deposited on boroaluminosilicate glass substrates using a 90 wt% In_2O_3, 10 wt% SnO_2 sputtering target at room temperature under a base vacuum pressure of 10^{-7} torr, followed by a 10-min anneal in Ar gas at 700 °C. Four samples were prepared with differing ITO thicknesses of d = 24, 53, 88, and 137 nm. The permittivity functions of the four films in the spectral range of 0.3–2.5 μm were obtained through spectroscopic ellipsometry measurements, using a combination of Drude and Gaussian models. In addition, root-mean-square roughnesses of 0.2, 0.26, and 1.3 nm were measured using atomic force microscopy for the 24-, 53-, and 137-nm-thick ITO films, respectively. Subsequently, a 200-nm layer of Ag was deposited on the ITO films using electron beam evaporation.

Since the Ag layer is opaque in the spectral range considered, the angular dependence of the reflection coefficient (Γ) was measured using a spectroscopic ellipsometer (J.A. Woollam, Inc.), and the absorption (A) was computed as $A = 1 - |\Gamma|^2$. For these measurements, the incident beam was coupled to the sample through a glass prism that was index matched to the glass substrate of the sample, with the Ag surface facing outward in a fashion similar to previous measurements [27]. The incidence angle was varied in a stepwise manner, and a reflection spectrum spanning the range from 6000 to 12 000 cm^{-1} (0.83 to 1.67 μm) was recorded for each angle.

The absorption spectra recorded at the incidence angles for which the maximum absorption was obtained are shown in Fig. 2, along with theoretical spectra computed using the three-medium Fresnel equation [26] (see Eq. (1) in Sec. III) using the measured ITO permittivity and literature values for the permittivity of Ag [28]. Good agreement is observed between experimental and theoretical results. The maximum absorption values measured for the four samples are between 99.79% and 99.98%. The instrumental limit of measuring zero reflectivity is 0.01%, and we estimate that other sources of error, such as uncertainties in the determination of the permittivity functions, the layer thicknesses, and the wavelengths, amount to an absorption uncertainty of 0.015%. A summary of the measured incidence angles, wavelengths, and values of maximum absorption for the four samples is presented in Table I, and a plot of the maximum absorption angle versus reduced thickness (d/λ_{PA}) from both experiment and theory is reported in Fig. 3. The wavelength at which PA was obtained increases with increasing sample thickness, while the PA angle decreases with increasing thickness.

A composite view of the experimental absorption spectra for the four samples is shown in the first column of Fig. 4. Each horizontal strip in this figure represents an absorption spectrum, measured at a particular incidence angle. The second column of Fig. 4 displays the theoretical results computed using the three-medium Fresnel equation [26]. These calculations are in good agreement with experimental results. On this figure, the PA point closest to the ENZ frequency is marked by a magenta cross (low-frequency PA). Careful inspection of the theoretical absorption maps shows the presence of a second PA condition that is beyond our experimental measurement range and is marked by a cyan square (high-frequency PA). We also show on the theoretical absorption maps a solid black curve, which is the locus of points depicting the behavior of the propagation constant (i.e., the real part of the complex modal wavenumber) of one of the electromagnetic eigenmodes of the system shown in Sec. IV. The trajectory of this particular eigenmode precisely crosses

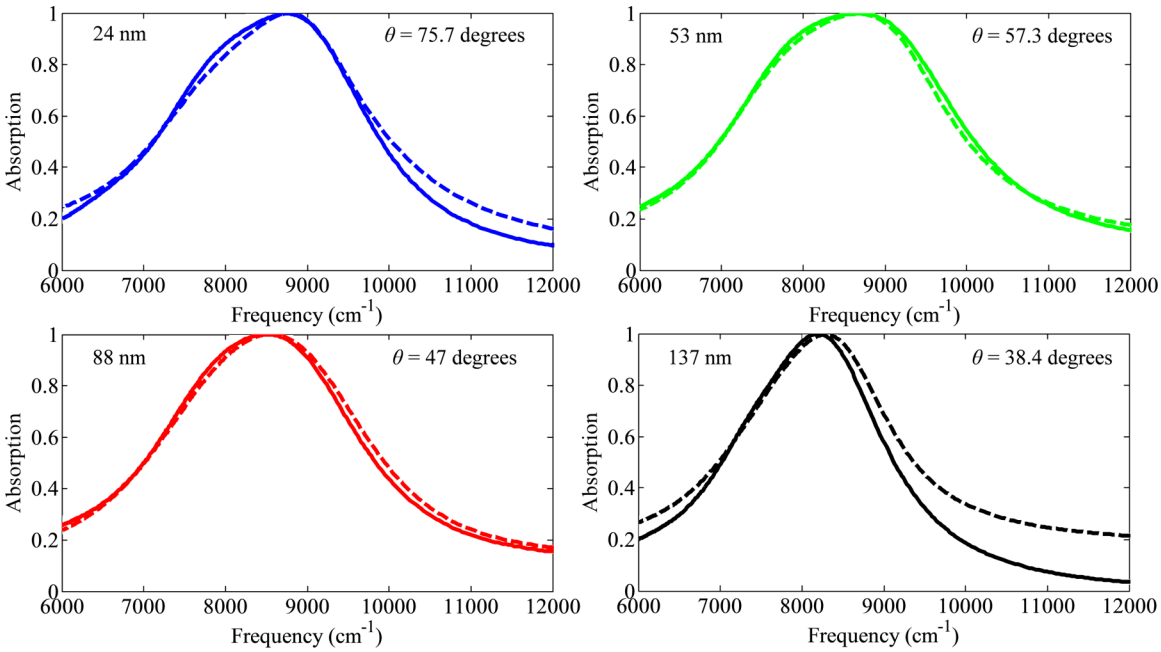

FIG. 2. (Color online) Comparison of measured PA profiles (solid) and calculated profiles using the three-medium Fresnel equation (dashed) for the four samples. The PA angle is explicitly indicated in each subplot.

both PA points (a deeper discussion of the modal dispersion will be provided in the next sections).

To understand the spatial dependence of the absorption, we performed full-wave finite-difference time-domain simulations (FDTD Solutions by Lumerical Solutions Inc.) using the PA conditions for the 53-nm sample as a representative case. In Fig. 5(a), we show the spatial profile of the absorption per unit length in units of inverse meters (proportional to $\varepsilon_0\varepsilon_2''|\mathbf{E}|^2/P_{\text{inc}}$ times the unit cell area used in simulation for convenience, with P_{inc} as the incident power) computed using the simulated total electric field $\mathbf{E}$. Inspection of Fig. 5(a) reveals that most of the energy is absorbed within the ITO layer. More quantitatively, numerical integration of the absorption per unit length in Fig. 5(a) along the thickness of the ITO film and the Ag region reveals that ~99% of the incident energy is absorbed within the deeply subwavelength ITO film and the remaining power dissipation (~1%) occurs in the Ag. Furthermore, the absorption per unit length is at maximum at the glass/ITO interface and drops monotonically throughout the thickness of the film, as shown in Ref. [24]. Compared to the ITO single pass absorption of about 5%, the absorption enhancement factor is about 20. Figure 5(b) shows the enhancements of the squared magnitude of the z component of the electric field that are observed within the ITO layer in the vicinity of the ENZ frequency. As also discussed in Ref. [29] for a subwavelength ENZ layer sandwiched between two silica domains, the maximum field enhancement does not occur at $\text{Re}(\varepsilon) = 0$ (indicated by a solid white line), where an enhancement of $|E_z|^2 \approx 4$ is observed (in the simulations, the total incident field strength is 1 V/m), but rather at a larger frequency. At the PA frequency (indicated by a dashed white line), which is slightly larger than the $\text{Re}(\varepsilon) = 0$ frequency, the enhancement is approximately $|E_z|^2 \approx 5$. A maximum enhancement of $|E_z|^2 \approx 7$ is observed at a somewhat higher frequency.

TABLE I. The experimental conditions for which PA was obtained for each of the four samples, showing the ITO thickness d, the ENZ wavelength λ_{ENZ}, the PA wavelength λ_{PA}, the PA incidence angle θ_{PA}, the real (ε_2') and imaginary (ε_2'') parts of the ITO permittivity at θ_{PA}, and the experimental absorption value A. The values of λ_{ENZ}, and of ε_2', and ε_2'' at λ_{PA} for each sample were obtained using ellipsometry measurements for each ITO film.

d (nm)	λ_{ENZ} (μm)	λ_{PA} (μm)	θ_{PA} (degrees)	ε_2'	ε_2''	A (%)
24	1.31	1.14	75.7	0.74	0.44	99.79
53	1.30	1.15	57.3	0.606	0.49	99.98
88	1.30	1.17	47	0.584	0.46	99.96
137	1.32	1.22	38.4	0.478	0.41	99.96

III. PA IN SUBWAVELENGTH FILMS: SIMPLE THEORETICAL FRAMEWORK

In this section we present a simple theoretical analysis of the conditions required to achieve PA in subwavelength films.

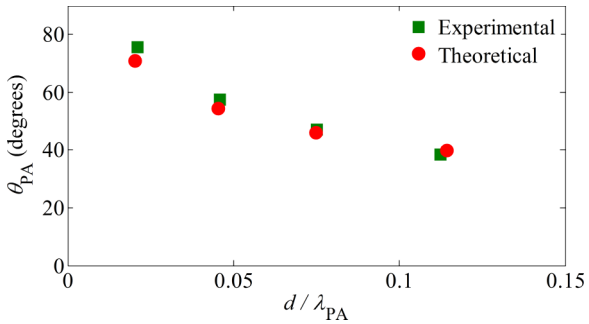

FIG. 3. (Color online) Experimental (green squares) and theoretical (red circles) angles of the observed PA points versus the reduced ITO thickness.

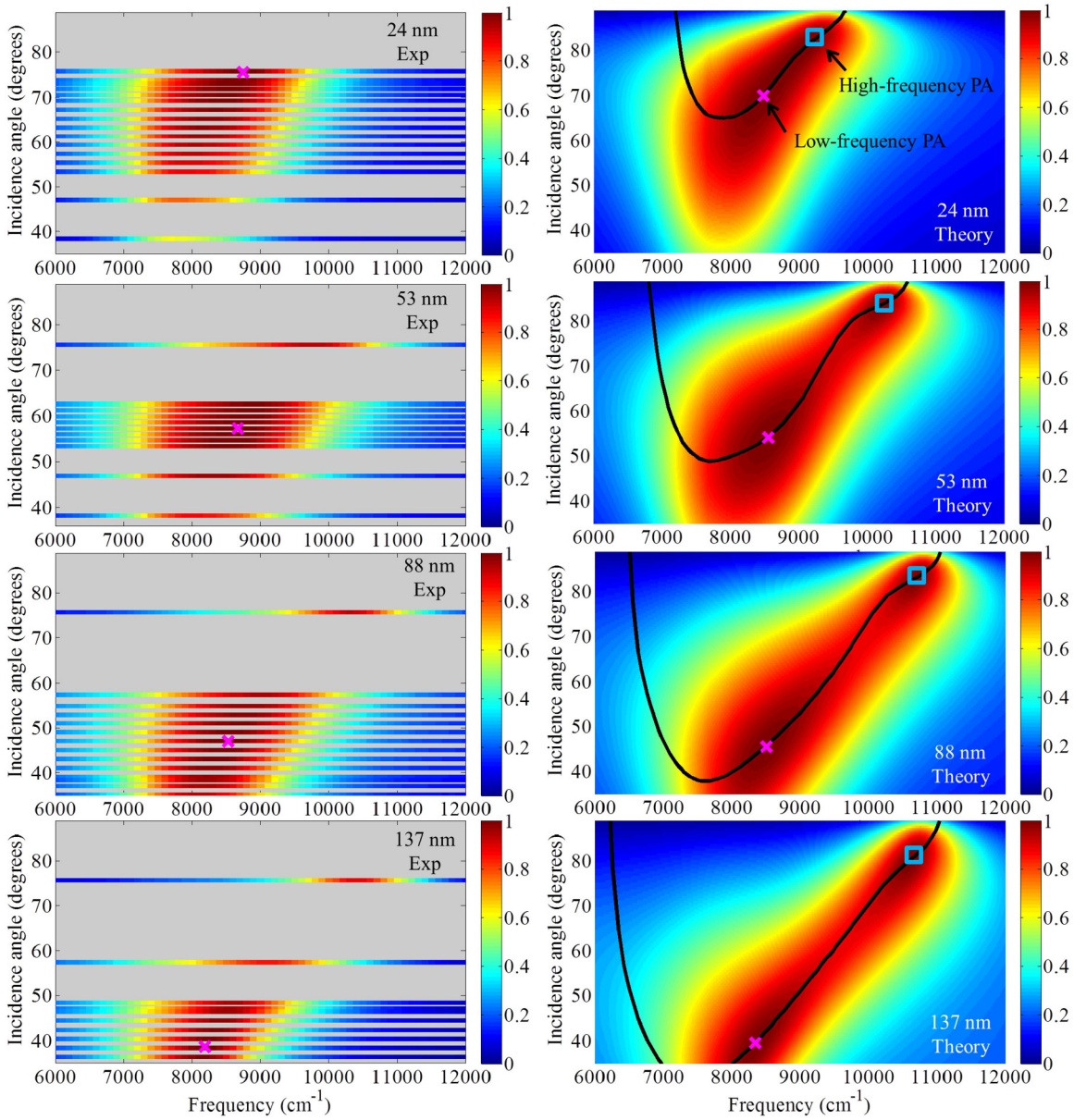

FIG. 4. (Color online) Comparison of measured angular and frequency dependence absorption profile of the four samples comprising ITO with $d = 24$, 53, 88, and 137 nm on Ag. The first column displays the raw experimental spectra at several discrete angles, and the second column shows results calculated from Eq. (1) using the experimental permittivity function for ITO and literature values for the permittivity of Ag [28]. The calculated absorption maps show two PA conditions that are indicated with magenta crosses and cyan squares. On these maps, we superimpose a solid black curve, which is the locus of points depicting the behavior of the propagation constant of one of the electromagnetic eigenmodes of the system shown in Sec. IV.

This will be followed in subsequent sections by more rigorous numerical analyses of the PA phenomenon. Consider the three-medium structure shown in Fig. 1. Media 1, 2, and 3 are the ambient dielectric, the low-permittivity material, and the metallic substrate with relative permittivities of ε_1, ε_2, and ε_3, respectively. The reflection coefficient Γ of such a structure is given by the standard three-medium layer Fresnel equation [26] (a time harmonic convention of the kind $\exp(-i\omega t)$ is implied):

$$\Gamma = \frac{r_{12} + r_{23}e^{2i\phi}}{1 + r_{12}r_{23}e^{2i\phi}} \tag{1}$$

where r_{ij} is the reflection coefficient of the ij interface, with $i, j = 1,2,3$; d is the layer thickness; and $\phi = k_{z2}d$ is the single pass phase shift across the low-permittivity layer. The longitudinal wavenumber k_{z2} is related to the component of the wavenumber parallel to the interface by the relation $k_{z2}^2 = \varepsilon_2 k_0^2 - k_x^2$, where $k_x = k_0\sqrt{\varepsilon_1}\sin\theta$ and k_0 and θ are the free-space wavenumber and the (real) incident angle, respectively.

For simplicity, we will begin by assuming medium 3 to be a perfect electric conductor (PEC), which implies that $r_{23} = -1$. In this case, we see from Eq. (1) that the reflection coefficient will vanish when $r_{12} = e^{2i\phi}$ (leading to the PA condition). If medium 2 exhibits loss, then physical solutions corresponding to $\Gamma = 0$ can be found. Assuming a p-polarized incidence and that the thickness of medium 2 is deeply subwavelength

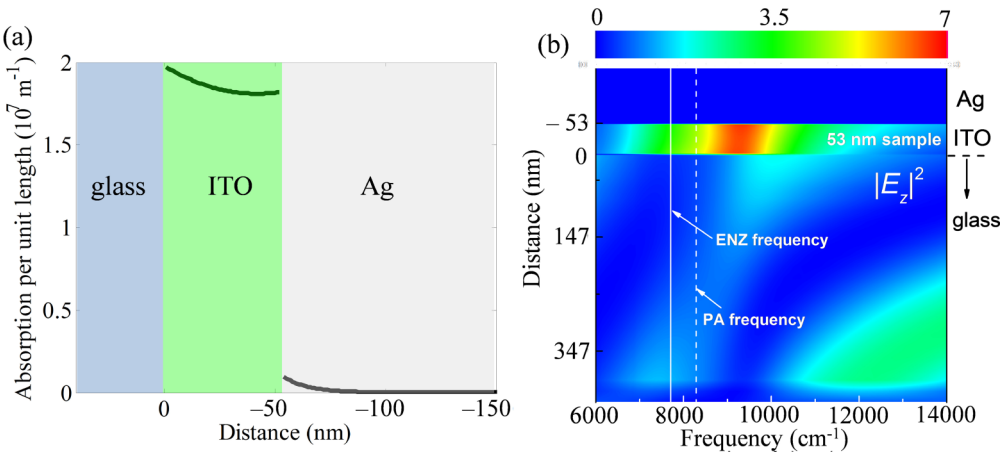

FIG. 5. (Color online) (a) The spatial profile of the absorption per unit length in units of inverse meters for the 53-nm sample at the PA frequency. Most of the energy is absorbed within the ITO layer. (b) The spatial distribution of the squared magnitude of the z component of the electric field versus frequency, showing ENZ-related field intensity enhancements. The maximum field enhancement is at a larger frequency than the frequency for which $\mathrm{Re}\,(\varepsilon) = 0$, in agreement with previous investigations [29].

(i.e., ϕ is small), the condition $r_{12} = e^{2i\phi}$ can be rewritten as [24]

$$\frac{k_{z2}^2 d}{\varepsilon_2} = i\frac{k_{z1}}{\varepsilon_1}. \tag{2}$$

Using $k_{z2}^2 = \varepsilon_2 k_0^2 - k_x^2$ and noting that ε_2 is a complex quantity, we can equate the real and imaginary parts of Eq. (2), to obtain, after some manipulation, the following PA conditions:

$$\sqrt{\varepsilon_1}\sin\theta_{\mathrm{PA}} = \sqrt{\frac{\varepsilon_2'^2 + \varepsilon_2''^2}{\varepsilon_2'}} \tag{3}$$

$$\frac{2\pi d_{\mathrm{PA}}}{\lambda_{\mathrm{PA}}} = \frac{\varepsilon_2'\cos\theta_{\mathrm{PA}}}{\sqrt{\varepsilon_1}\varepsilon_2''}. \tag{4}$$

We can further combine Eqs. (3) and (4) to obtain

$$\frac{2\pi d_{\mathrm{PA}}}{\lambda_{\mathrm{PA}}} = \left[\frac{\varepsilon_2'^2 + \varepsilon_2''^2}{\varepsilon_1^{3/2}\varepsilon_2''}\right]\frac{1}{\tan\theta_{\mathrm{PA}}\sin\theta_{\mathrm{PA}}}, \tag{5}$$

which is identical to the expression obtained using different considerations in Ref. [23]. To be consistent with the choice of small ϕ that led to Eq. (2), the acceptable choices for the parameters in Eqs. (4) and (5) must lead to a deep subwavelength film thickness. Thus, if the permittivity functions are such that the prefactor of Eq. (5) is not small, then extremely oblique angles must be used to maintain the thin film condition. Furthermore, the thickness d_{PA} will approach zero if, simultaneously, ε_2' and ε_2'' approach zero in such a manner that the prefactor of Eq. (5) approaches zero (i.e., if ε_2' approaches zero faster than ε_2'').

Inspection of Eqs. (3) and (4) reveals the conditions that the complex permittivity ε_2 must satisfy if PA is to be achieved in the deep subwavelength limit. From Eq. (4) we see that PA is possible only when $\varepsilon_2' > 0$. Therefore, the frequency at which PA occurs is larger than the ENZ frequency f_{ENZ}, defined as $\varepsilon_2'(f_{\mathrm{ENZ}}) = 0$, in agreement with what was indicated in Fig. 5(b). We obtain two further conditions the permittivity must satisfy by requiring that the incidence angle in Eq. (3) remains real:

$$\varepsilon_2'' < \frac{\varepsilon_1}{2} \tag{6}$$

$$\frac{\varepsilon_1}{2} - \sqrt{\frac{\varepsilon_1^2}{4} - \varepsilon_2''^2} \leqslant \varepsilon_2' \leqslant \frac{\varepsilon_1}{2} + \sqrt{\frac{\varepsilon_1^2}{4} - \varepsilon_2''^2} \tag{7}$$

Figure 6 shows the two bounds given by Eqs. (6) and (7). The shaded region between the red and the blue lines indicates an area where PA solutions can be found. All four samples described in Sec. II are within the shaded region, as indicated by the green squares. We emphasize that the solution shown in Fig. 6 was obtained in the PEC approximation and therefore only serves as a starting point for assessing the possibility of PA.

IV. ORIGIN OF PA 1: REAL-FREQUENCY/COMPLEX-WAVENUMBER MODAL DISPERSION DIAGRAMS

To unravel the physical origin of the PA conditions observed in Sec. II, we investigate the eigenmodes of the

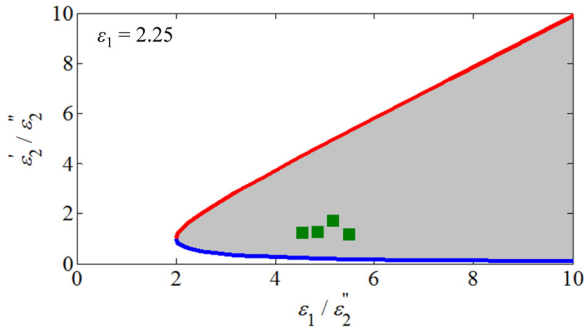

FIG. 6. (Color online) Upper (red) and lower (blue) bounds of $\varepsilon_2'/\varepsilon_2''$ given by Eqs. (6) and (7). The gray shaded region indicates the area where PA solutions can be found. The parameters of the four ITO samples studied here are shown in green squares. All analyzed designs fall within the PA region.

three-medium structure. While other theoretical methods such as critical coupling theory [30–32] or partial wave sums [19] could be used to analyze this system, we find the ability to locate the eigenmodes in the complex-wavenumber or complex-frequency plane extremely informative. Of primary interest are modes that lie close to the real-frequency or real-wavenumber axes, since these will couple most strongly to the incoming plane waves [33,34]. Furthermore, by monitoring the modal dispersion diagrams variation as a function of layer thickness or constituent material permittivities, we can systematically modify the structure to move the modes to desired locations [15,17]. In this section we compute the real-frequency/complex-wavenumber modal dispersion diagrams of modes supported by the three-medium structure, while in the next section we consider the complementary calculation of the real-wavenumber/complex-frequency dispersion diagrams.

Assuming a reference plane at the center of the ITO layer, the real-frequency/complex-wavenumber dispersion diagrams can be obtained by finding the complex roots of the equation $Z_t = Z_u + Z_d = 0$ for p-polarized waves, where $Z_u = \frac{A_2 Z_1 + B_2}{C_2 Z_1 + D_2}$ is the wave impedance of medium 1 transferred to the ITO center, $Z_d = \frac{A_2 Z_3 + B_2}{C_2 Z_3 + D_2}$ is the wave impedance of medium 3 transferred to the ITO center, and A_2, B_2, C_2, and D_2 are the $ABCD$ parameters of the ITO layer [35]. The longitudinal wavenumber k_{zn} in the nth media can then be computed using $k_{zn}^2 = k_n^2 - k_x^2$. Then, to find the eigenmodes, we fix the (real) frequency and find the (complex) transverse wavenumber ($k_x = \beta_x + i\alpha_x$) by calculating the roots of $Z_t = Z_u + Z_d = 0$. For p-polarized waves, the characteristic impedance of each layer becomes $Z_n = \frac{k_{zn}}{\omega \varepsilon_0 \varepsilon_n}$ and $k_n^2 = k_0^2 \varepsilon_n$, where ε_0 is the absolute permittivity of free space and ω is the angular frequency. (Modal dispersion diagrams can equivalently be determined by finding the complex roots of the denominator of Eq. (1).) Application of this procedure leads to four eigenmodes for each frequency, and each eigenmode is associated with a particular choice of signs for $\pm k_{z1}$ and $\pm k_{z3}$ [25]. In general, these four modes correspond to bound or

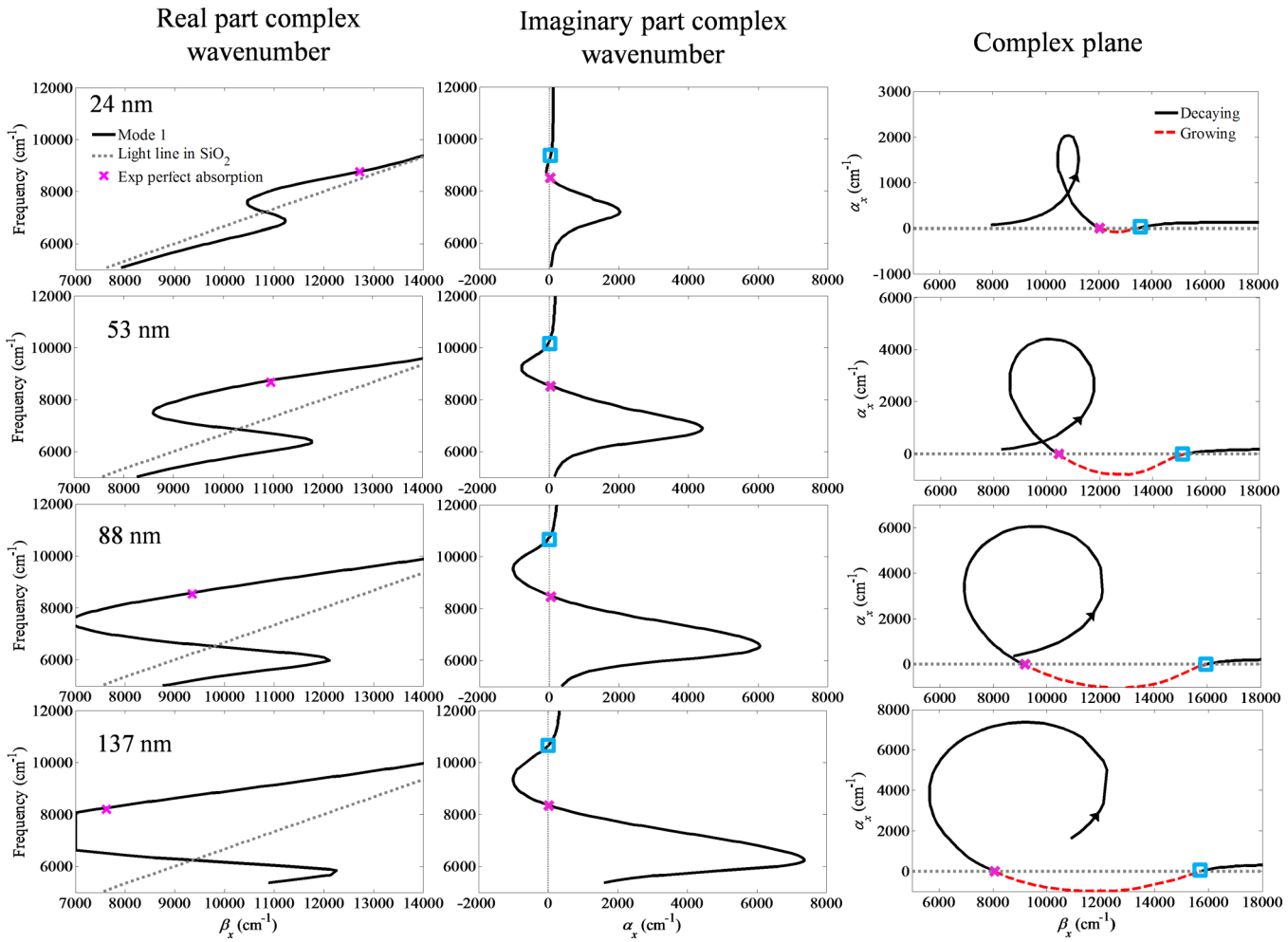

FIG. 7. (Color online) Real-frequency/complex-wavenumber modal dispersion diagrams pertaining to the four samples comprising ITO with d = 24, 53, 88, and 137 nm. The first column shows the frequency/propagation constant dispersion, the second column shows the frequency/attenuation constant dispersion, and the third column shows the dispersion diagram in the complex-wavenumber plane. Portions of these dispersions shown in column 1 were previously shown as black lines in column 2 of Fig. 4. In the first column, the experimental data points representing PA of the four samples are shown as magenta crosses. The dotted gray line represents the light line in medium 1. In the second and third columns, the two PA conditions are marked with magenta crosses and cyan squares, as done in Fig. 4. In the third column, the arrows indicate the direction of increasing frequency and the dotted gray line represents the real axis, i.e. $\alpha_x = 0$.

leaky waves of the structure, with incoming or outgoing wave propagation in the bounding half spaces (i.e., media 1 and 3). In the following, we retain only the particular eigenmode that we have found to be associated with the PA process.

Application of this numerical procedure leads to the dispersion diagrams depicted in Fig. 7 for the four samples investigated in this paper. As mentioned above, only one mode is retained in Fig. 7 since it plays a key role in explaining both PA conditions observed in Fig. 4. The first column of Fig. 7 shows the dependence of the propagation constant β_x (i.e., the real part of the complex modal wavenumber) on frequency, while the second column shows the frequency dependence of the attenuation constant α_x (i.e., the imaginary part of the complex modal wavenumber). The third column maps the dispersion diagram in the complex $\beta_x - \alpha_x$ plane. Inspection of the dispersion curves reveals that the amplitude of the switchback region and the attenuation constant both increase with increasing thickness. Furthermore, we observe that the attenuation constant crosses zero twice for each film thickness, an important condition to explain PA that will be discussed next. This is equivalent to the mode trajectory crossing the real axis of the complex plane twice, as is seen in the third column of Fig. 7.

The mode shown in Fig. 7 is obtained with a sign choice for k_{z1} that leads to incoming wave character in medium 1 for all frequencies. At low frequencies this mode is bound (i.e., exponentially decaying in medium 1, solid black in third column of Fig. 7), but with increasing frequency the trajectory of the mode in the complex $\beta_x - \alpha_x$ plane crosses the real axis and the mode becomes unbound (i.e., leaky; dashed red line in third column of Fig. 7). As the frequency continues to increase, the mode recrosses the real axis and again becomes bound (solid black in third column of Fig. 7). The points where this mode crosses the real axis are the PA points, marked with magenta crosses and cyan squares for convenience in both the second and the third columns of Fig. 7. At these points, the field in medium 1 is neither growing nor decaying; rather, it is the field of an incoming plane wave. Thus, at these points the field structure of this mode, which is an exact solution to Maxwell's equations, is indistinguishable from the field structure of an incoming and totally absorbed plane wave—PA. Thus, at these points (and in their close vicinity) a plane wave can phase match to the mode in the manner described in Refs. [33,34]. The sign choices required for the physically measured reflectivity ($+k_{z1}$ and $+k_{z3}$) differ from the sign choices for the mode whose dispersion is shown in Fig. 7 ($-k_{z1}$ and $+k_{z3}$) by the choice of sign for k_{z1}. As was shown in Ref. [14], $\Gamma(k_{z1}) = \Gamma^{-1}(-k_{z1})$ so that the pole of the reflection coefficient for the mode of interest becomes a zero of the experimental reflectivity, further justifying the overlap of the modal dispersion with the PA points in Fig. 4. The existence of two PA points is fully consistent with the reflectivity maps shown in Fig. 4, which were calculated using the same parameters (the zero crossing points are again marked with magenta crosses and cyan squares). Due to experimental limitations of the incidence angle, we are only able to obtain experimental verification of the PA point near the frequency of 8500 cm^{-1}.

V. ORIGIN OF PA 2: COMPLEX-FREQUENCY/REAL-WAVENUMBER MODAL DISPERSION DIAGRAMS

In this section we present the complementary analysis of the PA process using complex-frequency/real-wavenumber modal dispersion diagrams. These dispersion diagrams can be obtained by using a method similar to that used in Sec. IV

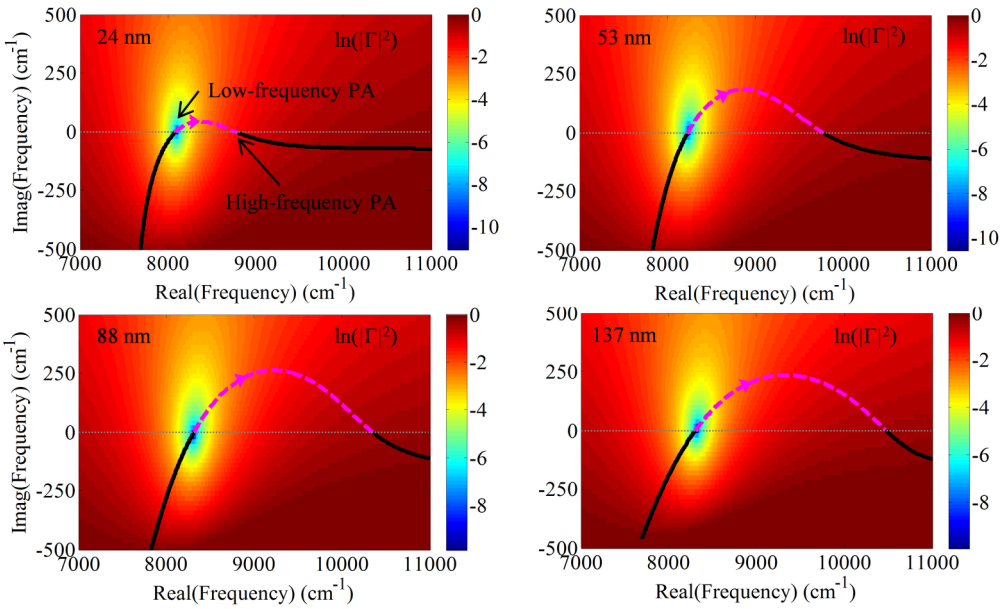

FIG. 8. (Color online) Complex-frequency maps of the natural logarithm of the reflectivity for the four samples computed from Eq. (1) at the PA incident angle. The zero reflectivity point (blue dot) represents the PA point. The solid and dashed lines are the dispersion diagrams of one eigenmode of the three-medium structure for increasing incidence angle indicated by the arrows. A solid line indicates a mode decaying in both medium 1 and 3, and a dashed line indicates a mode decaying in medium 3 and growing in medium 1. As observed in Fig. 4, we again achieve two PA points around 8500 and 10 000 cm^{-1} in correspondence with crossing of the $\text{Im}(\omega) = 0$ axis.

by finding the complex-frequency roots of the denominator of Eq. (1) for real k_x. As done in Sec. IV, we will retain only the relevant mode, computed using the sign choices $-k_{z1}$ and $+k_{z3}$, of the four possible modes that can be computed (the dispersion diagrams of all possible sign choices are reported in the Appendix for one sample). In these calculations, the dielectric functions of the ITO samples and Ag were approximated with complex Drude models since frequency-dependent permittivity values are required for complex frequencies. In Fig. 8, we show a complex-frequency map of the natural logarithm of the reflectivity calculated from Eq. (1) at the low-frequency PA angle of each sample. For arbitrary angles, the zero reflectivity point will not lie on the real axis. However, for angles that correspond to the experimentally determined PA angles, the PA point can be seen as a small blue region (blue dot) on the real axis (Fig. 8). Superimposed on the reflectivity map is the trajectory of the mode that is the complex-frequency analog of the mode described in Sec. IV. Again, we observe that the mode trajectory crosses the real axis in two locations, and for the maps shown here, the low-frequency crossing directly coincides with the zero of the reflectivity. (If the reflectivity maps were calculated for the conditions corresponding to the high-frequency PA, then the blue dots would be located at the points where the trajectories cross the real axis at higher frequencies; see the Appendix.) In agreement with the results of Sec. IV, two PA points are observed, and the wavenumber and frequency values of the PA points (which are real at these locations) agree with the corresponding values obtained from the complex-wavenumber analysis. Furthermore, in agreement with the results of Sec. IV, the locations where the mode trajectory crosses the real axis correspond to points at which the field of the mode corresponds to an incoming plane wave in medium 1, and the overall field profile is indistinguishable from the fields occurring for PA.

VI. CONCLUSION

We have provided an experimental demonstration that single beam directional PA can be achieved using deep subwavelength films of low-permittivity materials on metal substrates. Furthermore, we have shown that in the PA process, essentially all incoming energy is absorbed in the thin film material, not in the metallic substrate. While the results obtained in this paper specifically relate to ITO thin films, it is clear that similar behavior should be expected for any material with similar dielectric properties in any frequency range. For example, the PA behavior described in this paper is fully consistent with the results of Refs. [22,23], and explains why the absorption observed in those papers became stronger as the frequency was increased above the ENZ frequency. Thus, our results further expand the list of possible material candidates for use in PA applications to include other diluted plasmas, such as other conducting oxides; heavily doped semiconductors; restrahlen materials just above the longitudinal optical phonon frequencies; and correlated electron materials such as vanadium dioxide.

We have provided simple analytical formulas that relate material parameters to regions where PA solutions can be found and therefore can be used as a starting point for assessing the possibility of PA. We have further analyzed the electromagnetic eigenmodes of the layered structure from two complementary viewpoints and have shown that PA arises due to the behavior of a particular eigenmode of the system. Although in general this mode exhibits an unphysical field profile, it is nevertheless an exact solution of Maxwell's equations. Importantly, the mode field profile becomes identical to that of a totally absorbed incoming plane wave at the crossover between bound and leaky behavior, a property that was recognized in Ref. [25]. Hence, the PA process is also an exact solution to Maxwell's equations. Identification of the eigenmode responsible for PA will allow new designs to be obtained by adjusting material and structural parameters to force the trajectory of this mode to cross the real axis at desired locations. Furthermore, this procedure is general and can be employed in more complex multilayer systems. Interestingly, our analysis has revealed the existence of a second set of PA points, which are outside the accessible measurement range of our instrumentation. Thus, these results provide a new path for the design of custom absorber materials that do not rely on surface patterning or texturing and hence will be more appealing for device applications.

ACKNOWLEDGMENTS

The authors acknowledge stimulating discussions with Tom Tiwald, Mathias Schubert, Xiaodong Yang, and Zongfu Yu. This paper was supported by the US Department of Energy, Office of Basic Energy Sciences, Division of Materials Sciences and Engineering, and the work was performed, in part, at the Center for Integrated Nanotechnologies, an Office of Science User Facility operated for the US Department of Energy, Office of Science. Sandia National Laboratories is a multiprogram laboratory managed and operated by Sandia Corporation, a wholly owned subsidiary of Lockheed Martin Corporation, for the US Department of Energy's National Nuclear Security Administration under Contract No. DE-AC04-94AL85000.

APPENDIX: DETAILED COMPLEX-FREQUENCY/REAL-WAVENUMBER MODAL DISPERSION DIAGRAMS

In this Appendix, we use the method described in Secs. IV and V to compute the complex-frequency/real-wavenumber modal dispersion diagrams of all modes supported by the three-medium structure for the 53-nm sample. Figure 9 shows four complex-frequency maps of the natural logarithm of the reflectivity corresponding to four incidence angles. As mentioned in Sec. V, for arbitrary angles the zero reflectivity point (blue dot) does not lie on the real axis but does lie on the real axis at the PA angle. This can be clearly observed in Fig. 9, where the position of the blue dot depicting the reflectivity minimum moves in the complex-frequency plane as the incidence angle is varied. Superimposed on the reflectivity maps are the trajectories of the modes (without distinguishing between bound or leaky for simplicity and clarity of presentation) computed with the following sign choices: (1) $+k_{z1}$ and $+k_{z3}$ (dashed white), (2) $-k_{z1}$ and $+k_{z3}$ (dotted green), (3) $+k_{z1}$ and $-k_{z3}$ (solid

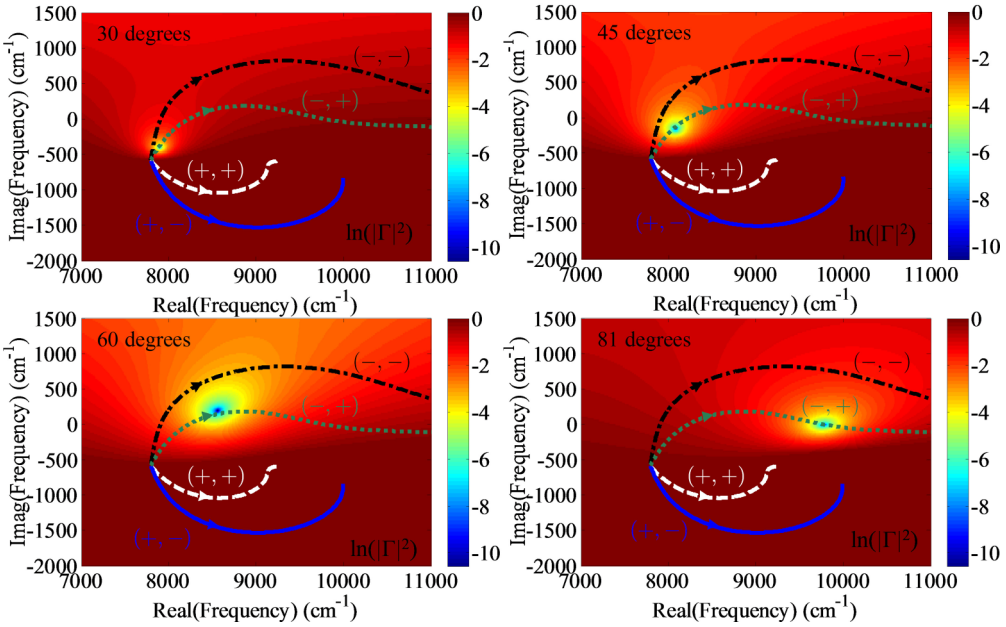

FIG. 9. (Color online) Complex-frequency maps of the natural logarithm of the reflectivity for the 53-nm-thick sample computed from Eq. (1) for four incidence angles. Only the trajectory of the eigenmode computed using the sign choice $-k_{z1}$ and $+k_{z3}$ follows the reflectivity minima for different incidence angles, further confirming that this eigenmode is associated with the PA process.

blue), and (4) $-k_{z1}$ and $-k_{z3}$ (dashed-dotted black). We observe that only the trajectory of the dotted green mode, computed with the sign choice $-k_{z1}$ and $+k_{z3}$, follows the locus of the reflectivity minima for various incidence angles, which clearly demonstrates that this particular eigenmode is responsible for the PA process.

[1] Y. Cui, Y. He, Y. Jin, F. Ding, L. Yang, Y. Ye, S. Zhong, Y. Lin, and S. He, Laser Photonics Rev. **8**, 495 (2014).

[2] K. Aydin, V. E. Ferry, R. M. Briggs, and H. A. Atwater, Nat. Comm. **2**, 517 (2011).

[3] F. Yi, E. Shim, A. Y. Zhu, H. Zhu, J. C. Reed, and E. Cubukcu, Appl. Phys. Lett. **102**, 221102 (2013).

[4] N. I. Landy, S. Sajuyigbe, J. J. Mock, D. R. Smith, and W. J. Padilla, Phys. Rev. Lett. **100**, 207402 (2008).

[5] N. Liu, M. Mesch, T. Weiss, M. Hentschel, and H. Giessen, Nano Lett. **10**, 2342 (2010).

[6] Z. Fang, Y.-R. Zhen, L. Fan, X. Zhu, and P. Nordlander, Phys. Rev. B **85**, 245401 (2012).

[7] Q. Cheng, T. J. Cui, W. X. Jiang, and B. G. Cai, New J. Phys. **12**, 063006 (2010).

[8] H.-T. Chen, Optic. Express **20**, 7165 (2012).

[9] P. Spinelli, M. A. Verschuuren, and A. Polman, Nat. Comm. **3**, 692 (2012).

[10] T. Søndergaard, S. M. Novikov, T. Holmgaard, R. L. Eriksen, J. Beermann, Z. Han, K. Pedersen, and S. I. Bozhevolnyi, Nat. Comm. **3**, 969 (2012).

[11] H. Shin, M. F. Yanik, S. Fan, R. Zia, and M. L. Brongersma, Appl. Phys. Lett. **84**, 4421 (2004).

[12] J. S. Q. Liu and M. L. Brongersma, Appl. Phys. Lett. **90**, 091116 (2007).

[13] V. Shah and T. Tamir, Optic. Comm. **23**, 113 (1977).

[14] M. Neviere and P. Vincent, J. Optic. **11**, 153 (1980).

[15] V. Shah and T. Tamir, Optic. Comm. **37**, 383 (1981).

[16] A. Amittay, P. D. Einziger, and T. Tamir, Appl. Phys. Lett. **38**, 754 (1981).

[17] Y. D. Chong, L. Ge, H. Cao, and A. D. Stone, Phys. Rev. Lett. **105**, 053901 (2010).

[18] W. Wan, Y. Chong, L. Ge, H. Noh, A. D. Stone, and H. Cao, Science **331**, 889 (2011).

[19] M. A. Kats, R. Blanchard, P. Genevet, and F. Capasso, Nat. Mater. **12**, 20 (2013).

[20] E. F. C. Driessen and M. J. A. d. Dood, Appl. Phys. Lett. **94**, 171109 (2009).

[21] M. A. Kats, D. Sharma, J. Lin, P. Genevet, R. Blanchard, Z. Yang, M. M. Qazilbash, D. N. Basov, S. Ramanathan, and F. Capasso, Appl. Phys. Lett. **101**, 221101 (2012).

[22] R. P. Godwin and M. M. Mueller, Appl. Optic. **12**, 1276 (1973).

[23] B. Harbecke, B. Heinz, and P. Grosse, Appl. Phys. A **38**, 263 (1985).

[24] S. Feng and K. Halterman, Phys. Rev. B **86**, 165103 (2012).

[25] J. J. Burke, G. I. Stegeman, and T. Tamir, Phys. Rev. B **33**, 5186 (1986).

[26] M. Born and E. Wolf, *Principles of Optics: Electromagnetic Theory of Propagation, Interference, and Diffraction of Light* (Cambridge University Press, Cambridge, UK, 1999).

[27] T. S. Luk, I. Kim, S. Campione, S. W. Howell, G. S. Subramania, R. K. Grubbs, I. Brener, H.-T. Chen, S. Fan, and M. B. Sinclair, Optic. Express **21**, 11107 (2013).

[28] E. D. Palik, *Handbook of Optical Constants of Solids* (Academic Press, San Diego, CA, 1991).

[29] S. Campione, D. de Ceglia, M. A. Vincenti, M. Scalora, and F. Capolino, Phys. Rev. B **87**, 035120 (2013).

[30] H. A. Haus, *Waves and Fields in Optoelectronics* (Prentice Hall, Englewood Cliffs, NJ, 1984).
[31] A. Yariv, Electron. Lett. **36**, 321 (2000).
[32] J. W. Yoon, W. J. Park, K. J. Lee, S. H. Song, and R. Magnusson, Optic. Express **19**, 20673 (2011).
[33] A. Hessel and A. A. Oliner, Appl. Optic. **4**, 1275 (1965).
[34] D. de Ceglia, S. Campione, M. A. Vincenti, F. Capolino, and M. Scalora, Phys. Rev. B **87**, 155140 (2013).
[35] D. M. Pozar, *Microwave Engineering* (John Wiley and Sons, Hoboken, NJ, 2011).